Journal of Energy Storage 89 (2024) 111686

Contents lists available at ScienceDirect

Journal of Energy Storage

journal homepage: www.elsevier.com/locate/est

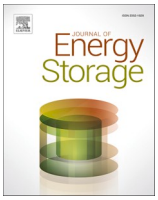

Research papers

# Efficiency and power density analysis on phase change material-based ocean thermoelectric generator for underwater vehicle

Yanhu Chen *, Zesheng Yao, Bingzhe Chen *, Canjun Yang, Gul Muhammad, Qingchao Xia

*The State Key Laboratory of Fluid Power & Mechatronic Systems, Zhejiang University, 310027, PR China*

ARTICLE INFO

*Keywords:*
Power generation
Ocean thermal energy
Efficiency analysis
Power density
Phase change material

ABSTRACT

Utilizing the volume change of phase change materials (PCM) to realize ocean thermal energy-electric energy conversion is a promising method. The PCM-based ocean thermal engine has the potential to solve the energy limitation problem of underwater vehicles. In this paper, detailed numerical and experimental research on the thermoelectric conversion process was conducted. A numerical model was proposed for thermal–mechanical and mechanical–electrical energy conversion process; and an experimental set-up was built for system identification and model validation. The efficiency and power density of the ocean thermoelectric generator under different configuration were analyzed numerically. Finally, a prototype was developed and tested. Results showed that: (1) In deep water area, the optimal pre charging pressure is 10 MPa for achieving maximum power density and this configuration is a compromise among the efficiency, phase change time and weight; (2) In shallow area, to achieve maximum output power, pressure range for power generation should be set to 15-20 MPa, while the motor speed need to be set to 6000 rpm; (3) the total energy conversion efficiency and the power density of the prototype in the lab test was 0.453 % and 21.58 mW/kg, respectively, attaining state-of-the-art performance compared to the current literature.

## 1. Introduction

The ocean covers 71 % of the Earth's surface area [1], and has substantial influence on the global environment and human society [2]. Therefore, research in marine science is of great significance. Ocean observation equipment serves as a crucial tool for marine science. However, the limited battery capacity restricts the operating life of the ocean observation equipment. Utilizing in-situ renewable energy for energy replenishment of batteries is an effective method to break this limitation [3].

Marine renewable energy mainly includes tidal energy [4], wave energy [5], thermal energy, etc. Among them, ocean thermal energy is widely distributed, structurally stable, and has abundant reserves, making it an ideal energy source for underwater observation equipment. Currently, for small observation equipment, the mainstream way of harvesting ocean thermal energy is to use solid–liquid phase change materials (PCM) [6]. Webb et.al [7] first proposed a design scheme for underwater vehicle buoyancy regulation using PCM to harvest ocean thermal energy. The thermal engine changed the volume of the external bladder by the volume change of PCM, achieving the sinking and floating motion of the vehicle. In 1998, the thermal glider Slocum Thermal was developed and the lake trail was conducted in Seneca Lake where the vertical temperature difference reached 13 °C. Results showed the feasibility of the PCM-based engine. Subsequently, Jones et. al [8,9] optimized the wing and heat exchanger structure, and developed another two gliders, named Slocum WT01 and Slocum Drake, respectively. The sailing distance was further extended. Yang et.al [10] has proposed the thermal model of the PCM-based underwater thermal gliders, developed a prototype, and conducted the sea trial.

Subsequently, researchers proposed another improved engine: an internal power generation system was added to the original engine, for converting thermal energy into electrical energy and storing it in batteries. Although this indirect energy-conversion method incurs energy loss during the power generation process, the generated electrical energy can not only be used for buoyancy adjustment, but also for other carried power consuming modules and sensors. Chao et.al [11] conducted the first research on small-scale ocean thermoelectric power generation technology based on PCM, and integrated the ocean thermoelectric generators into ARGO buoys, named SOLO-TREC. The working depth of SOLO-TREC is 500 m, and the single cycle power generation reaches 6.1 kJ, realizing the energy self-supply of the buoy.

* Corresponding authors.
*E-mail addresses:* yanhuchen@zju.edu.cn (Y. Chen), bzchen@zju.edu.cn (B. Chen).

https://doi.org/10.1016/j.est.2024.111686
Received 21 January 2024; Received in revised form 30 March 2024; Accepted 9 April 2024
Available online 20 April 2024

**Nomenclature**

| | |
|---|---|
| $A_m$ | mushy zone constant (kg/(m$^3$·s)) |
| $B$ | buoyancy (N) |
| $c_p$ | specific heat (J/(kg·K)) |
| $C_F$ | inertial coefficient |
| $D$ | displacement (L) |
| $E$ | energy (J) |
| $g$ | gravitational acceleration (m/s$^2$) |
| $h$ | convective heat transfer coefficient (W/(m$^2$·K)) |
| $I$ | current (A) |
| $k_{eff}$ | equivalent thermal conductivity of PCM–copper foam composites (W/(m·K)) |
| $K$ | permeability (m$^2$) |
| $L$ | latent heat of fusion (J/kg) |
| $m$ | mass (kg) |
| $P_1$ | inlet pressure of the hydraulic motor (MPa) |
| $P_2$ | outlet pressure of the hydraulic motor (MPa) |
| $Q$ | flow rate (L/s) |
| $S$ | source term |
| $t$ | time (s) |
| $T$ | temperature (°C) |
| $U$ | voltage (V) |
| $U_c$ | relative uncertainty |
| $V$ | volume (L) |
| $\vec{V}$ | velocity (m/s) |

*Greek symbols*

| | |
|---|---|
| $\alpha$ | scale factor |
| $\beta$ | liquid fraction |
| $\gamma$ | thermal expansion coefficient of PCM (K$^{-1}$) |
| $\varepsilon$ | porosity of metal foam |
| $\eta$ | efficiency |
| $\mu$ | dynamic viscosity (N·s/m$^2$) |
| $\rho$ | density (kg/m$^3$) |
| $\sigma$ | absolute uncertainty of sensor measurement |
| $\omega$ | a small constant to prevent division by zero |

*Subscripts*

| | |
|---|---|
| *a* | effective value |
| *ac* | accumulator |
| *bat* | battery |
| *buo* | buoyancy |
| *c* | cold end |
| *E* | electrical |
| *f* | fluid |
| *F* | metal foam |
| *h* | hot end |
| *l* | liquid phase |
| *M* | mechanical |
| *s* | solid phase |
| *shell* | metal shell of heat exchangers |
| *T* | thermal |

*Abbreviations*

| | |
|---|---|
| PCM | phase change material |
| MF | metal foam |
| AC | alternating-current power |
| DC | direct-current power |
| PID | proportional integral derivative algorithm |

However, SOLO-TREC weighs up to 84 kg, which is larger in volume and weight than traditional buoys. Besides, in deep and distant sea environments, the energy consumption will increase, and the thermoelectric generator will not be able to maintain self-sufficiency. Haldeman et.al [12] developed the fourth generation of the Slocum thermal glider, named Slocum TREC, and realized the ocean thermoelectric conversion in glider, significantly improving the working life of the glider. The American company Seatrac has designed a thermoelectric conversion system SL1 for the Navis series profiler to supplement the electrical energy of the profiler. In 2019, the system completed 42 profile experiments with a maximum depth of 750 m in Hawaii. From a single profile cycle, the thermoelectric generators can output 7920 J of electrical energy [13].

Theoretical research on the energy conversion process of ocean thermal engines has also made significant progress. Carneiro et al. [14] proposed a simple dynamic model for the heat transfer between PCMs and the environment to calculate the efficiency of the cycle of the ocean thermal engine. Xia et al. [15] developed a heat transfer model for filling liquid-PCM mixture, and analyzed the effects of pressure and heat exchanger diameter on the phase change time. Wang et al. [16] used molecular dynamics methods to calculate the PCM phase change point, thermal conductivity, and specific heat under different temperature and pressure. Ma et.al [17] proposed a nonlinear model of the ocean thermal engine containing residual air, and analyzed the effects of air solubility in PCM, system pressure, and pre charging pressure of the accumulator on energy storage performance. Kim et al. [18] conducted numerical study on energy allocation with various types of motion and geometry of the ocean thermal engine. Liu et al. [19] proposed a theoretical model for a piston type ocean thermal engine and found that the output power of the engine system is positively correlated with nitrogen pressure, PCM volume, seawater velocity, and gliding angle of the vehicle. Chen et al. [20,21] conducted numerical and experimental research on the ocean thermal energy harvesting process using PCM–metal foam composites. Yao et al. [22] numerically analyze the phase change process of PCM in ribbed heat exchangers.

There are various forms of PCM-based ocean thermal engines. In this work, we mainly focuses on engines with installed power generation systems, and refers to this power generation system as a thermoelectric generator. Current studies on the efficiency of thermal engines primarily rely on theoretical analysis, neglecting the distinctive attributes of real power generation systems, and there is still insufficient modeling and experimental work on the thermoelectric generator in ocean thermal engines; furthermore, the existing available data of ocean thermoelectric generators in lake and sea trail often lacks comprehensiveness for conducting in-depth research on the internal energy conversion process. Therefore, there is still a significant knowledge gap that needs to be filled regarding the experimental characteristics of power generation process driven by ocean thermal energy. The main contribution of this paper is:

(1) Numerical models for the thermoelectric conversion process and power generation systems efficiency were established and experimentally validated;

(2) The power generation performance, including power density and energy efficiency, was analyzed through numerical simulations. Power generation strategies were proposed for different diving depths to maximize power density;

(3) A prototype of an ocean thermoelectric generator was developed and tested in the laboratory environment. Note that the experimental data includes detailed information about energy efficiency and power density, which is rare in previous literature. The power generation performance of the prototype was analyzed through experimental results.

The structure of this article is as follows: Section 2 introduces the working principle of an ocean thermoelectric heat engine; Section 3

elaborates on the numerical model of the thermoelectric conversion process and power generation system; Section 4 introduces the power generation experimental set-up and developed prototype system; Section 5 presents the results and discussion of the numerical and experimental study, which is mainly divided into three parts: (i) the power generation experimental set-up is used to identify the system and obtain the undetermined parameters in the numerical model; (ii) then, numerical research on the thermoelectric conversion process under different ocean environment is carried out, and the power generation strategies of the ocean thermoelectric generator is optimized; (iii) Finally, the pressure parameters of the prototype is set based on the numerical results and experiments are conducted in a laboratory environment.

## 2. Concept of PCM-Based Ocean thermoelectric generator

The schematic diagram of the ocean thermoelectric generator is shown in Fig. 2. The whole system consists of several heat exchangers, on/off valves, an accumulator, a generator, an external oil bladder, and an inner hydro-cylinder. The external oil bladder is immersed in seawater and is responsible for regulating the overall net buoyancy of the engine to control its descent and ascent, while the other components are distributed inside the engine. The inner hydro-cylinder is used to store sufficient hydraulic oil. When the whole system periodically shuttles between the warm and cold water layer, the PCM inside heat exchangers contracts and expands repeatedly, and the oil is pumped in and out through the heat exchangers. By this way, the ocean thermal energy is converted to other forms of usable energy. A working cycle can be divided into the following 5 steps:

(1) Initially, accumulator is in the high-pressure state. The system is at the ocean surface, and the PCM is in liquid phase. By opening the relevant valve, under the pressure of seawater, oil flows from the external oil bladder into the inner cylinder, causing the system to sink. (Fig. 2 (a));

(2) When reaching the cold water layer, PCM contracts due to solidification and heat exchangers suck oil from the inner hydro-cylinder (Fig. 2 (b));

(3) After the pressure inside the accumulator rises to a certain value, the corresponding on-off valve is opened, and hydraulic oil flows into the inner cylinder from the accumulator, driving the hydraulic motor and generator to rotate;

(4) When the system reaches the target depth, the pressure of the accumulator is released. Oil flows from the accumulator into the external oil bladder, increasing the system's buoyancy and starting to float upwards (Fig. 2 (d));

(5) The system float up to the ocean surface, and PCM volume expands due to melting. Therefore, the accumulator returns to a high-pressure state (Fig. 2 (e)).

## 3. Numerical modeling

In this section, thermoelectric energy conversion modeling is conducted by combining the power generation efficiency model with the overall working cycle of the engine. The energy conversion in ocean thermoelectric engines can be divided into two processes: (1) Thermal–mechanical energy conversion: PCM absorbs thermal energy, expands its volume, and causes the internal pressure of the accumulator to rise; (2) Mechanical–electrical energy conversion: By operating the on/off valve, the pressure of the accumulator is released, and oil flows out of the accumulator, driving the motor and generator to rotate, thereby outputting electrical energy. Based on the open-source software OpenFOAM [23], a corresponding solver has been developed to numerically solve the mathematical model in this section. Our code is available on GitHub.[1]

### 3.1. Thermal–hydraulic energy conversion model

The harvesting and storage process of ocean thermal energy occurs during the PCM melting stage; PCM expands and squeezes oil into the accumulator to complete energy storage. Due to the low thermal conductivity of traditional PCM, metal foam is inserted inside the heat engine system to increase the heat transfer rate [24]. The enthalpy-porosity method [25] was used to simulate the phase change process of PCM. Here, we did not describe the details of the modeling process, but directly list the control equations describing the heat transfer process of PCM-metal foam composites.

Continuity:

$$\nabla \bullet \vec{V} = 0 \tag{1}$$

Momentum

$$\frac{\rho_{PCM}}{\varepsilon}\frac{\partial \vec{V}}{\partial t} + \frac{\rho_{PCM}}{\varepsilon^2}\left(\vec{V}\cdot\nabla\right)\vec{V} = \frac{\mu}{\varepsilon}\nabla^2\vec{V} - \nabla P + \vec{S} \tag{2}$$

where $\rho_f$ is the density of the PCM, $\mu$ is the dynamic viscosity, $\varepsilon$ is the porosity of metal foam. The momentum source terms in the horizontal and vertical directions are given by:

$$S_x = -\frac{A_m(1-\beta)^2}{\beta^3+\omega}u - \frac{\mu}{K}u - \frac{\rho_f C_F}{\sqrt{K}}\left|\vec{V}\right|u \tag{3}$$

$$S_y = -\frac{A_m(1-\beta)^2}{\beta^3+\omega}v - \frac{\mu}{K}v - \frac{\rho_f C_F}{\sqrt{K}}\left|\vec{V}\right|v + \gamma_f\rho_f g\left(T_f - T_l\right) \tag{4}$$

where $K$ and $C_F$ are structural parameters related to copper foam. $A_m$ is the mushy zone constant which equals to 105, and $\omega$ is 0.001 to prevent division by zero. $\gamma_f$ is the thermal expansion coefficient of PCM and $\beta$ is the liquid fraction of PCM, defined as follows:

$$\begin{cases} \beta = 0 & T_f \le T_s \\ \beta = \dfrac{T_f - T_s}{T_l - T_s} & T_s < T_f < T_l \\ \beta = 1 & T_f \ge T_l \end{cases} \tag{5}$$

Energy:

$$\left[(1-\varepsilon)\rho_{MF}c_{pF} + \varepsilon\rho_{PCM}c_{pf}\right]\frac{\partial T}{\partial t} + \varepsilon\rho_{PCM}L\frac{d\beta}{dt} + \rho_f c_{pf}\left(\vec{V}\cdot\nabla\right)T = \nabla\cdot\left(k_{eff}\nabla T\right) \tag{6}$$

where $c_{pF}$ and $c_{pf}$ are the specific heat capacity of metal foam and PCM, respectively. $\rho_{MF}$ is the density of copper foam, $L$ is the latent heat of PCM and $k_{eff}$ is the equivalent thermal conductivity of PCM–metal foam composites.

The bottom is set as an adiabatic boundary condition, and the upper and side walls are set as convective heat transfer boundary conditions, as shown in Eqs. (7)–(9).

$$\left.\frac{\partial T}{\partial y}\right|_{y=0} = 0 \tag{7}$$

$$-\lambda\left.\frac{\partial T}{\partial y}\right|_{y=H} = \frac{T_\infty - T}{\frac{1}{h_1} + \frac{\delta_1}{\lambda_{shell}}} \tag{8}$$

[1] https://github.com/Yao-Zesheng/inconstantPressurePhaseChangeFOAM.git.

$$-\lambda\left.\frac{\partial T}{\partial x}\right|_{x=R}=\frac{T_\infty-T}{\frac{1}{h_2}+\frac{\delta_2}{\lambda_{shell}}} \tag{9}$$

The grid and time step independence analysis was conducted. The pressure range during power generation was set to 15-20 MPa. Three mesh sizes, 6400, 51,200, and 102,400 and two adaptive time step method is employed to solve the transient processes: (i) setting 1: the maximum Courant number is 1.0, and the maximum time step is 0.2 s; (ii) setting 2: the maximum Courant number is 0.5, and maximum time step is 0.1 s. As shown in Fig. 3, the results of using the three mesh sizes and two time steps are considerably similar.

Notably, in our previous work, the corresponding verification and experimental validation of the above numerical modeling was conducted. For details, refer to [21,22].

### 3.2. Hydraulic–electric energy conversion model

The nitrogen gas in the accumulator undergoes polytropic process and thus the pressure inside accumulator $P_a$ during power generation is given by:

$$P_a=\frac{P_{start}{V_{start}}^{n_e}}{\left(V_{start}+\int Q_a dt\right)^{n_e}} \tag{10}$$

where, $P_{start}$ is the pressure at which the accumulator starts generating electricity, $V_{start}$ is the volume of nitrogen gas at the beginning of the accumulator's power generation, $Q_a$ is the flow rate of oil flowing out of the accumulator and is consistent with the input flow rate of the hydraulic motor, $n_e$ is the polytropic exponent. Due to the relatively rapid pressure changes in the accumulator during the power generation process, gas can be considered as having no heat exchange with the environment and thus $n_e$ is set to 1.4.

The total volume of oil flowing out of the accumulator $V_{ac}$ during a power generation process is given by:

$$V_{ac}=\left(\frac{P_0{V_0}^{n_e}}{P_{end}-\Delta P_e}\right)^{\frac{1}{n_e}}-\left(\frac{P_0{V_0}^{n_e}}{P_{start}}\right)^{\frac{1}{n_e}}=\int_0^{t_e}Q_{ac}dt \tag{11}$$

where $P_0$ is the pre charging pressure of the accumulator, $V_0$ is the nominal volume of the accumulator, $P_{end}$ is the pressure of the accumulator at the end of power generation.

The power generation $E_e$ in a single cycle of the engine is given by:

$$E_e=\sum\nolimits_{i=1}^{j}\eta_E\int_0^{t_e^i}\left(P_1^i-P_2^i\right)Q_{ac}^i dt \tag{12}$$

where $j$ is the power generation time, $P_1^i$ and $P_2^i$ are the inlet and outlet pressure of hydraulic motor, respectively.

There are two situations in the power generation process: (i) hydraulic oil flows into the external oil bladder through the hydraulic motor (Fig. 1 (c)); (ii) Hydraulic oil flows into the inner cylinder through the hydraulic motor (Fig. 1 (d)). Situation (i) represents the buoyancy adjusting process, and the hydraulic motor outlet has a certain pressure. A portion of the mechanical energy in the accumulator is used to drive the total system from a submerged state to an upward floating state, while the remaining portion is converted into electrical energy; In situation (ii), the outlet pressure of the hydraulic motor is 0, and all mechanical energy is used for power generation. The amount of hydraulic oil required for buoyancy adjustment $V_{oil,buo}$ is proportional to the weight of the OTEng [11]:

$$V_{oil,buo}=\frac{\alpha M}{\rho_{oil}} \tag{13}$$

where $\alpha$ is the scale factor and is determined according to the following analysis: as the dive depth increases, the density of the seawater also gradually increases, resulting in an increase in the buoyancy force on the OTEng. The buoyancy difference between the sea surface and target dive depth $h$ is:

$$\Delta B(h)=\left[\rho_{seawater}(h)-\rho_{seawater}(0)\right]gV \tag{14}$$

$V_{oil,buo}$ must satisfy the Eqs. (24)–(25) to overcome the buoyancy difference caused by the change in sea water density.

$$B=\rho_{seawater}(h)V_{oil,buo}g\geq\left[\rho_{seawater}(h)-\rho_{seawater}(0)\right]gV \tag{15}$$

where $V_{oil,buo}$ is the volume of the hydraulic oil flowing into the external blader, and $B$ is the change in buoyancy from the diving state to the floating state. According to Eqs. (22)–(25), $\alpha$ satisfies the following relationship:

$$\alpha\geq\rho_{oil}\frac{\rho_{seawater}(h)-\rho_{seawater}(0)}{\rho_{seawater}(h)\rho_{seawater}(0)} \tag{16}$$

Next, the power generation efficiency model was developed. The

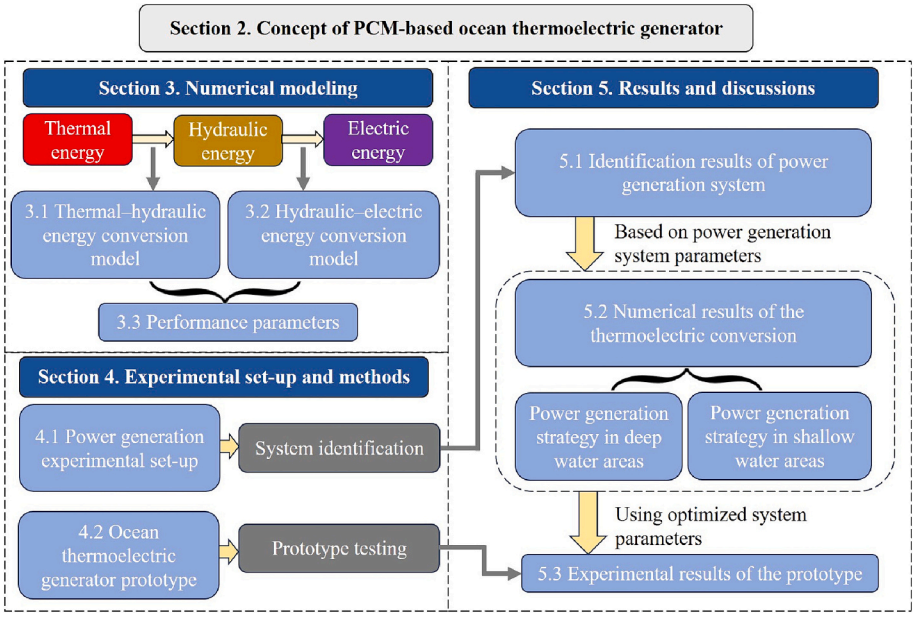


**Fig. 1.** The content and logical relationship of each section in this paper.

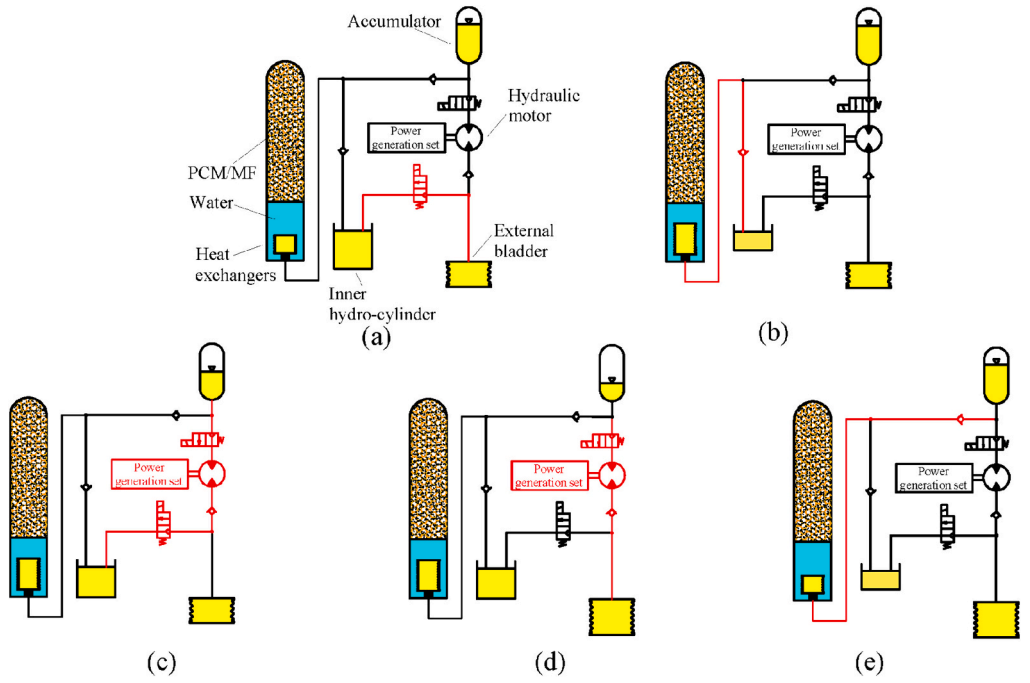


**Fig. 2.** Operating processes of the PCM-based ocean thermoelectric generator. (a) Diving, (b) PCM freezing, (c) Power generation, (d) buoyancy adjusting and (e) PCM melting.

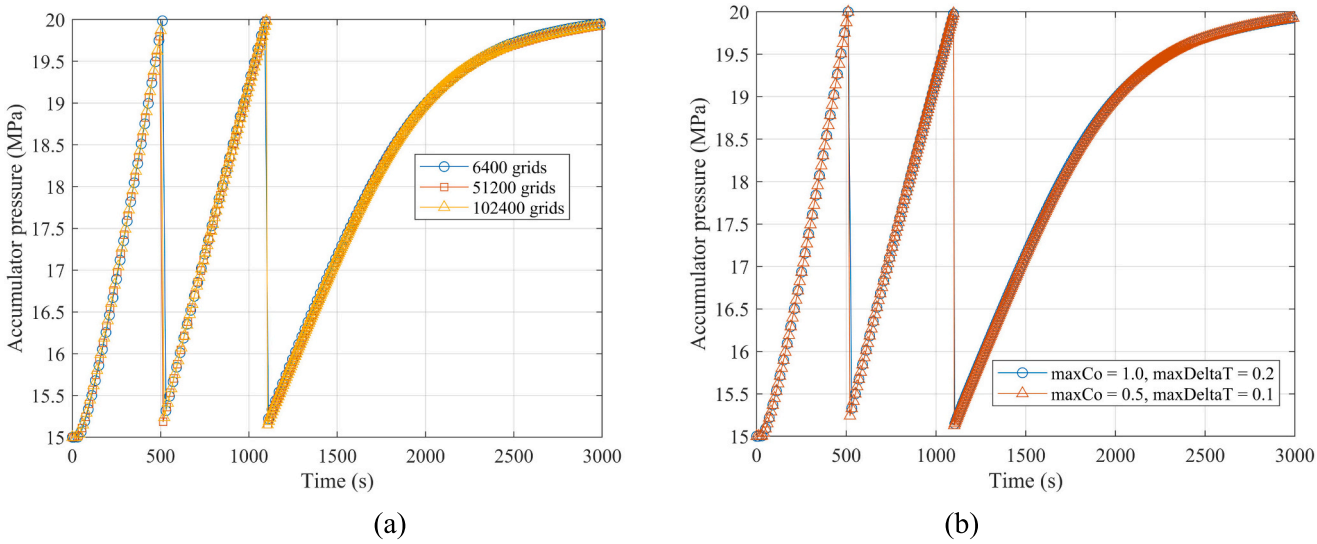


**Fig. 3.** Results of the grid size and time step sensitivity tests: (a) grid size sensitivity test, (b) time step sensitivity test.

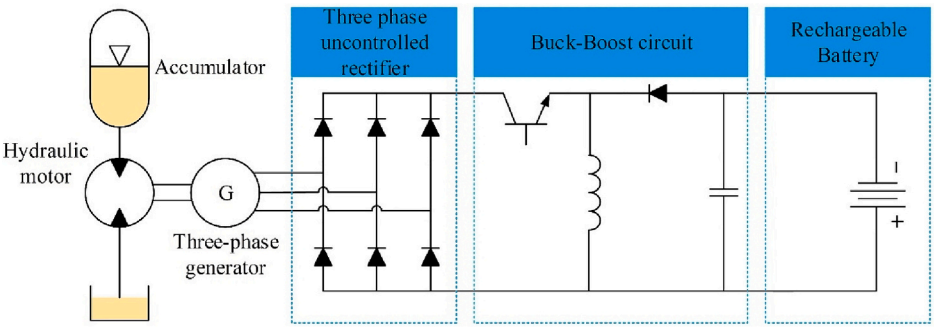


**Fig. 4.** Schematic diagram of power generation system.

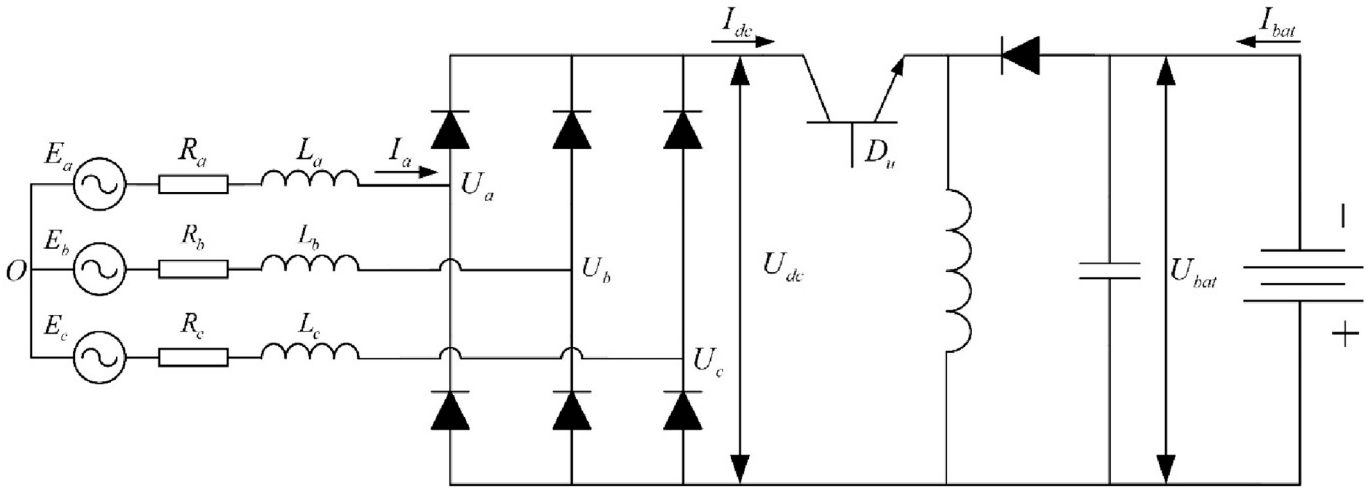


**Fig. 5.** Equivalent circuit on the three-phase generator side.

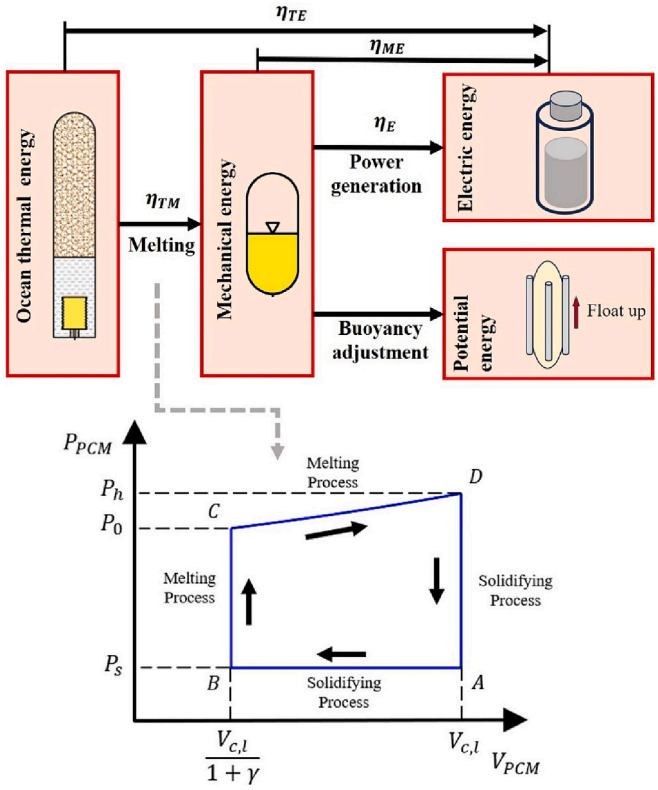


**Fig. 6.** Energy flux of the ocean thermoelectric generator.

function of the power generation system is to convert the mechanical energy stored in the accumulator into electrical energy stored in the battery. As shown in Fig. 4, the designed power generation system consists of a hydraulic motor, three-phase generator, three-phase uncontrolled rectifier, Buck Boost circuit, and rechargeable battery. Through the hydraulic motor, the three-phase generator is driven by high-pressure oil from the accumulator to output alternating-current (AC) power. The AC power is converted into direct-current (DC) power through a three-phase uncontrolled rectifier. The battery is charged through a Buck-Boost circuit, which can adjust the charging current of the battery.

The power loss of hydraulic motors is divided into two parts: volumetric and mechanical loss. The power loss of these two parts is characterized by volumetric efficiency $\eta_V$ and mechanical efficiency $\eta_M$. According to [26], $\eta_M$ and $\eta_V$ are given by:

$$\eta_M = 1 - \frac{2\pi C_1}{\Delta P \cdot D} n - \frac{2\pi C_0(\Delta P + 2P_2)}{\Delta P} \tag{17}$$

$$\eta_V = \frac{1}{1 + C_V \frac{\Delta P + 2P_2}{\mu_{oil} D \cdot n}} \tag{18}$$

The actual flow rate $Q_p$ of the hydraulic motor can be obtained based on the speed $n$ and displacement $D$:

$$Q_p = \frac{nD}{\eta_V} \tag{19}$$

The mechanical energy in the accumulator is converted into electrical energy and stored in the battery. The definition of electric energy conversion efficiency $\eta_E$ is as follows:

$$\eta_E = \frac{U_{bat} I_{bat}}{(P_1 - P_2) Q_p} \tag{20}$$

where $U_{bat}$ and $I_{bat}$ denotes the charging voltage and current of the battery.

The driving torque of hydraulic motors $T_M$ is given by:

$$T_M = \frac{(P_1 - P_2) D}{2\pi} \eta_M \tag{21}$$

When modeling three-phase generators, the following assumptions are adopted:

(1) The three-phase windings of the generator are connected in a star shape and symmetrically distributed;
(2) The air gap magnetic field of the generator exhibits a sinusoidal distribution, and the self-inductance and mutual inductance of each winding are constant;
(3) The following factors is ignored: the core magnetic resistance, magnetic field saturation of the generator stator and rotor, internal eddy current, hysteresis losses of the generator, spatial harmonics;
(4) The speed change rate during the power generation process is significantly smaller than the current change rate inside the three-phase generator. Therefore, the power generation process can be regarded as a quasi-steady state process, where the speed of the hydraulic motor and three-phase generator is approximately constant within a time interval $\Delta t$.

Therefore, the equivalent circuit of the three-phase generator is

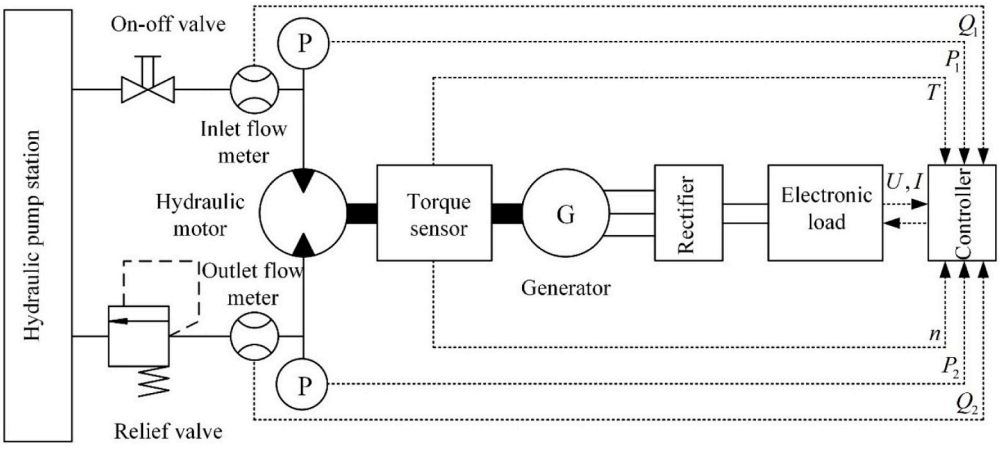


(a)

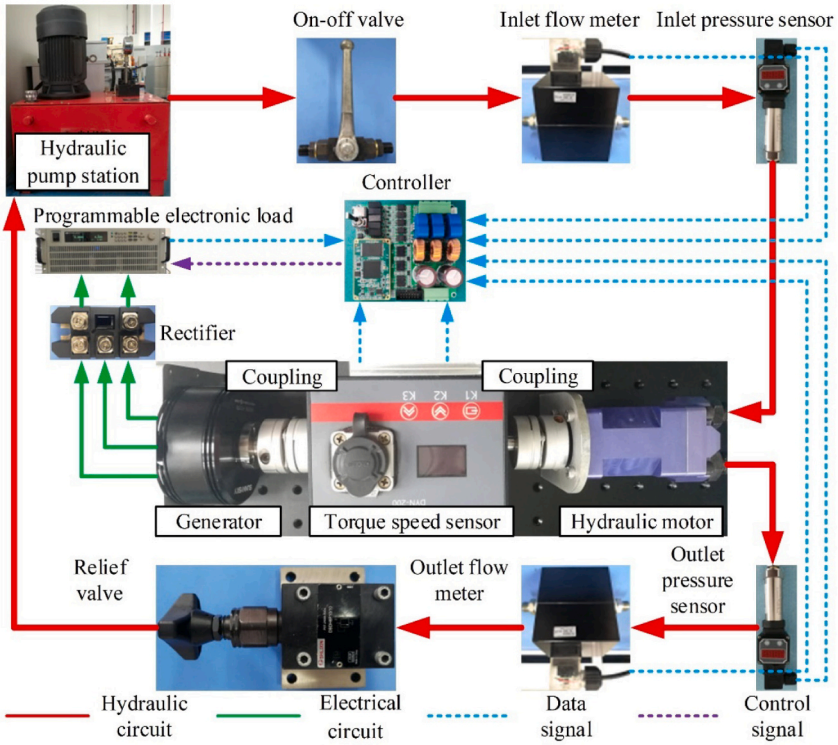


(b)

**Fig. 7.** (a) Diagram and (b) physical map of the power generation experimental set-up.

shown in Fig. 5:

The electromagnetic torque of the generator is:

$$\vec{T}_{em} = p\vec{\psi} \times \vec{I} \tag{22}$$

where $p$ is the polar logarithm, $\vec{\psi}$ is the magnetic flux vector of the stator, and $\vec{I}$ is the current vector.

And the effective value of $\vec{T}_{em}$ can be expressed as:

$$T_{ema} = K_A I_a \tag{23}$$

where $I_a$ is the effective value of phase current $\vec{I}$, $K_A$ is the torque coefficient.

Resistance torque $T_G$ is given by:

$$T_G = T_{ema} + T_{ini} \tag{24}$$

where $T_{ini}$ denotes the torque generated by hydraulic motors and generators due to mechanical factors.

The effective value of electromotive force generated by single-phase winding $E_a$ is given by:

$$E_a = 4.44fNk\Phi = K_V n \tag{25}$$

where $f$ the frequency of the induced electromotive force, $N$ the total number of turns per phase of the generator's single-layer winding in

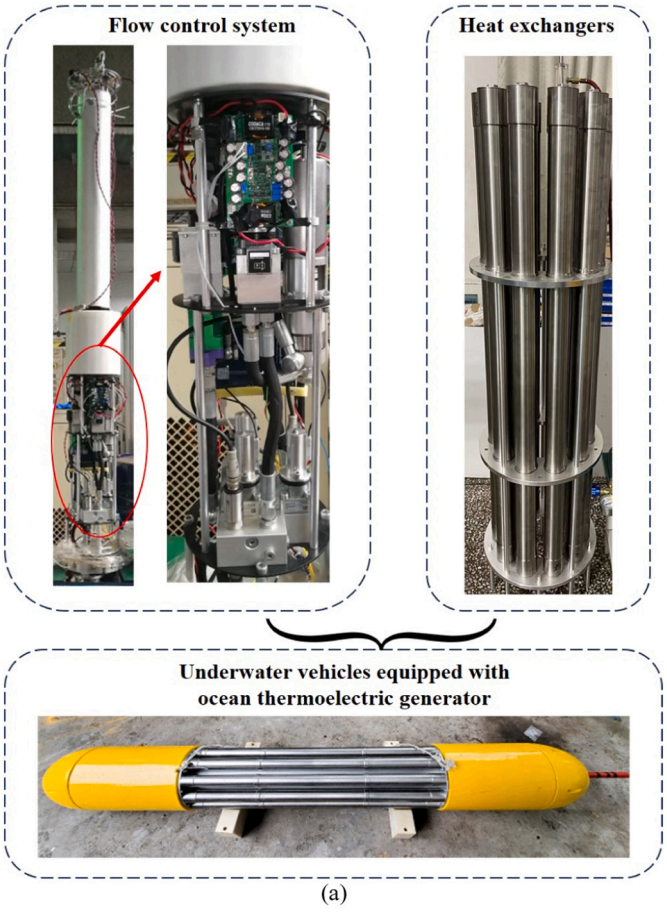


**Fig. 8.** Physical image of the (a) prototype and (b) the corresponding experimental set-up.

series, $k$ the fundamental winding factor, $\Phi$ magnetic flux, and $K_V$ is the velocity constant.

The instantaneous value of single-phase voltage input by an uncontrollable rectifier $\widetilde{U}_a$ is given in Eq. (26),

$$\widetilde{U}_a = \widetilde{E}_a - \widetilde{I}_a R_a - L_a \frac{d\widetilde{I}_a}{dt} \tag{26}$$

where $R_a$ and $L_a$ are the winding resistance and inductance, respectively. $\widetilde{E}_a$ and $\widetilde{I}_a$ denote the instantaneous values of the induced electromotive force and phase current of the single-phase winding, respectively.

Therefore, the effective value of the single-phase voltage input to the uncontrollable rectifier $U_a$ is:

$$U_a = E_a - I_a R_a = K_V n - K_I I_a \tag{27}$$

where $K_V$ and $K_I$ are proportional coefficients.

The voltage $U_{dc}$ and current $I_{dc}$ output from the DC side of the uncontrollable rectifier are given in Eqs. (28)–(29):

$$U_{dc} = \frac{3\sqrt{6}}{\pi} U_a \tag{28}$$

$$I_{dc} = \frac{\pi}{\sqrt{6}} I_a \tag{29}$$

The conversion efficiency of the Buck Boost circuit is $\eta_B$, and the charging current of the battery is given by:

$$I_{bat} = \frac{U_{dc} I_{dc} \eta_B}{U_{bat}} \tag{30}$$

When the system reaches steady state, the driving torque and resistance torque of the hydraulic motor are equal. Therefore, in steady state, phase current $I_a$ and charging current of the battery $I_{bat}$ are given by Eqs. (31)–(32):

$$I_a = \frac{(P_1 - P_2)D}{2\pi K_A} \eta_M - \frac{T_{ini}}{K_A} \tag{31}$$

$$I_{bat} = \frac{3(K_V n - I_a R_a) I_a \eta_B}{U_{bat}} \tag{32}$$

Based on the above analysis, the parameterized efficiency model of power generation system can be obtained as follows:

$$\eta_E = \frac{k_1 n^2 + (k_2 \Delta P + k_3 P_2 + k_4) n + (k_5 \Delta P + k_6 P_2 + k_7)^2}{k_8 \Delta P \cdot n + k_9 \Delta P^2 + (k_{10} P_2 + k_{11}) \Delta P} \tag{33}$$

where $k_1$–$k_{11}$ are constant parameters that need to be determined through further experiments. Eq. (33) shows that under the condition of constant pressure, there exists an optimal speed that maximizes the energy conversion efficiency of the energy storage and power generation system, and this optimal working point is the maximum efficiency point.

### 3.3. Performance parameters

The energy conversion process of ocean thermoelectric generator is shown in Fig. 6. Through the solidification and melting of PCM, ocean thermal energy is converted into mechanical energy in the accumulator. A portion of the mechanical energy is used for buoyancy regulation of the total system, driving the system periodically shuttle through the ocean thermocline. This part of the energy is ultimately converted into the gravitational potential energy of the system. And the remaining mechanical energy is converted into electrical energy through the generator.

The total thermal energy absorbed by PCM in a single profile cycle is given by

$$E_T = c_{ps} m_{PCM} (T_s - T_c) + m_{PCM} L + c_{pl} m_{PCM} (T_h - T_l) \tag{34}$$

where $c_{ps}$ and $c_{pl}$ are the specific heat of the solid and liquid phase PCM, respectively. $T_h$ is the surface water temperature.

Thermal to mechanical energy conversion efficiency $\eta_{TM}$, generation efficiency $\eta_{ME}$ are defined in Eqs. (31)–(32):

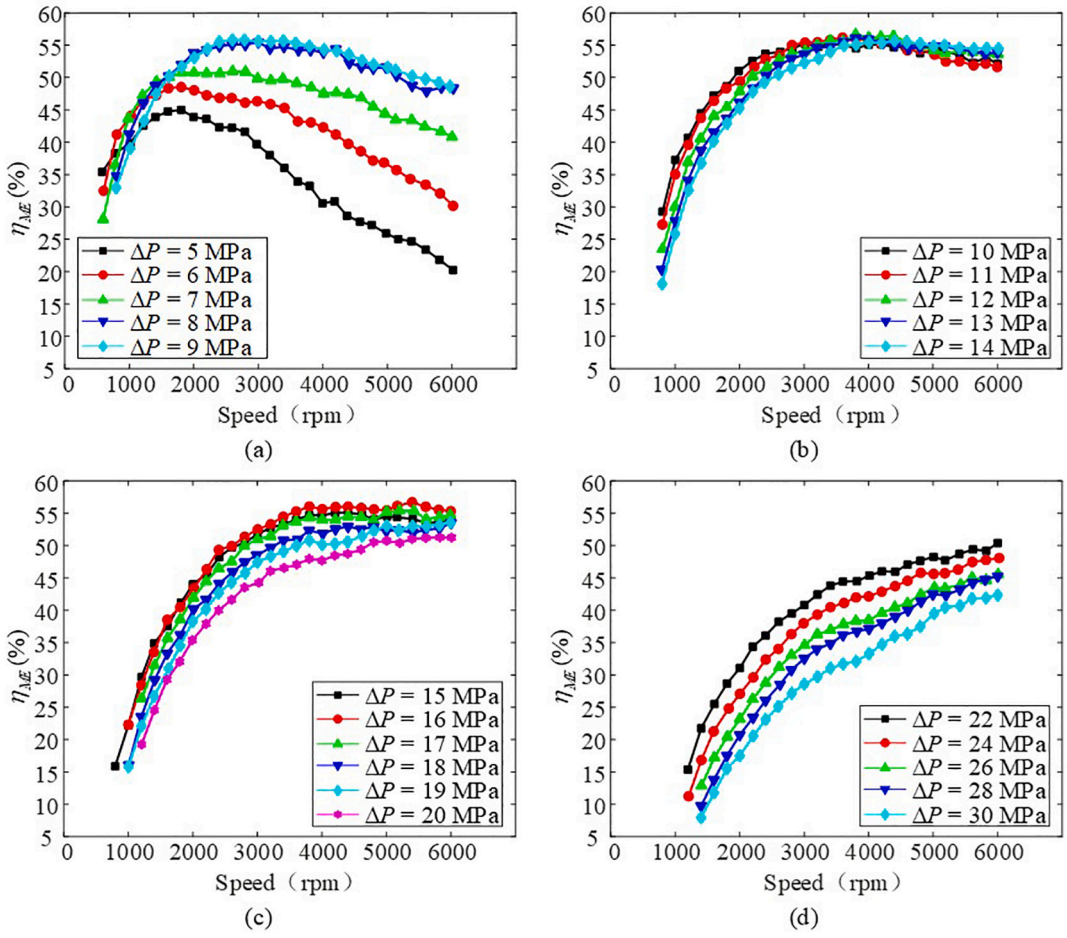


**Fig. 9.** The variation curve of generation efficiency $\eta_E$ with pressure difference and speed under outlet pressure of 0 MPa. (a) Pressure difference within the range of 5–9 MPa, (b) Pressure difference within the range of 10–14 MPa, (c) Pressure difference within the range of 15–20 MPa, and (d) Pressure difference within the range of 22–30 MPa.

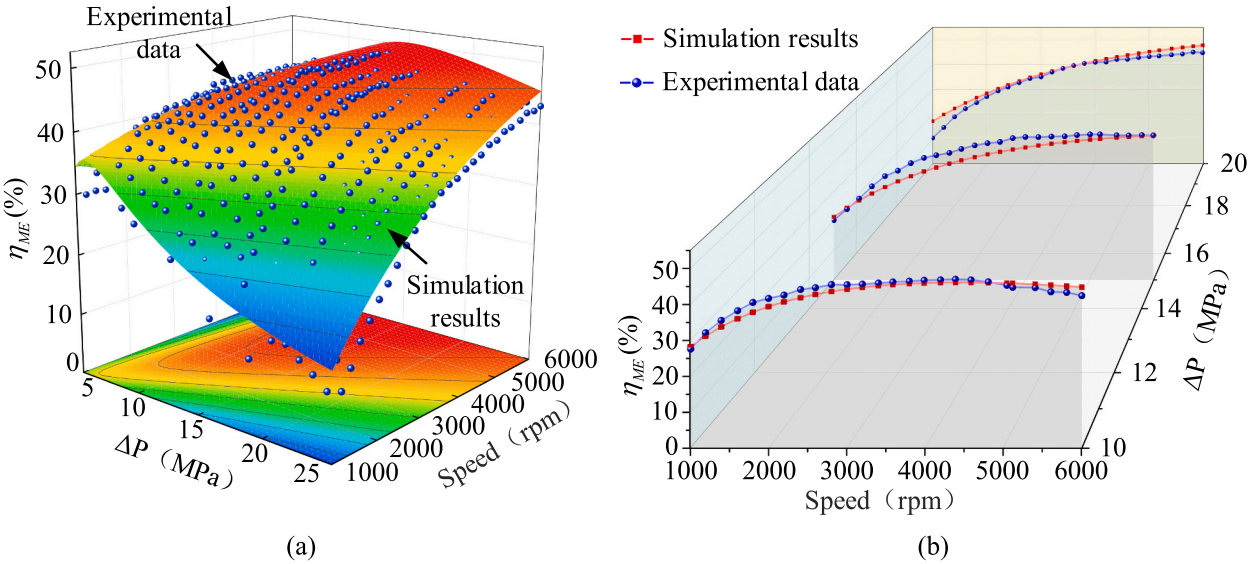


**Fig. 10.** Comparison of experimental data and model simulation results for outlet pressure of 5 MPa. (a) Comparison of experiments and simulations of all data, (b) Comparison of experiments and simulations at pressure differentials of 10 MPa, 15 MPa and 20 MPa.

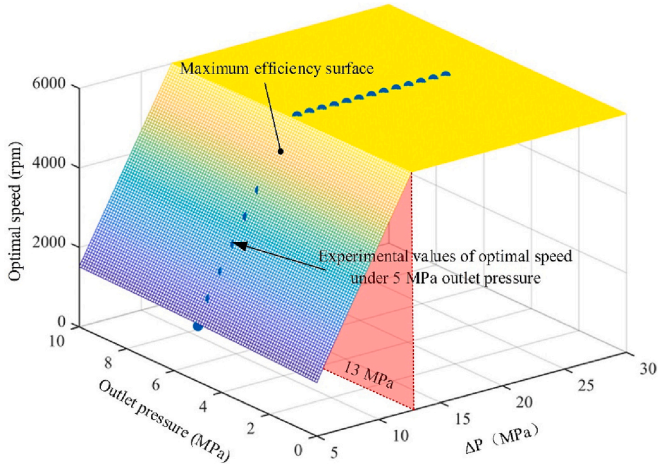


**Fig. 11.** Optimal speed under different pressure differentials and outlet pressures.

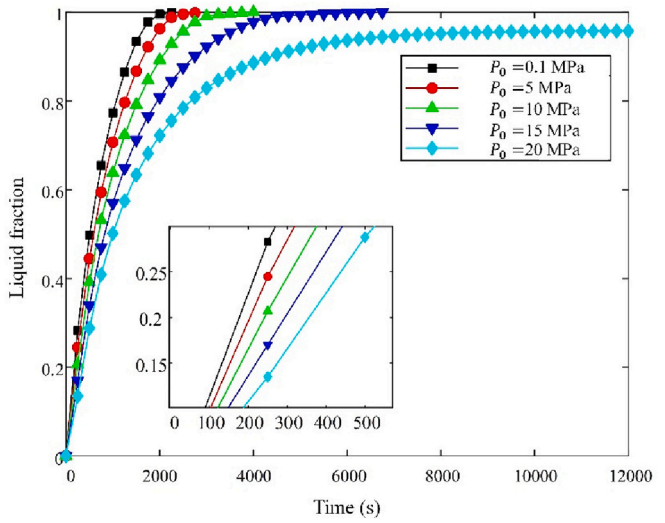


**Fig. 12.** Influence of pre charging pressure on the melting process under the single power generation strategy.

$$\eta_{TM} = \frac{E_M}{E_T} = \frac{\sum_{i=1}^{j} \int_0^{t_e^i} P_1^i Q_{ac}^i dt}{c_{ps} m_{PCM}(T_s - T_0) + m_{PCM} L + c_{pl} m_{PCM}(T_e - T_l)} \tag{35}$$

$$\eta_{ME} = \frac{E_e}{E_M} = \frac{\sum_{i=1}^{j} \eta_E \int_0^{t_e^i} (P_1^i - P_2^i) Q_{ac}^i dt}{\sum_{i=1}^{j} \int_0^{t_e^i} P_1^i Q_{ac}^i dt} \tag{36}$$

Therefore, the conversion efficiency from thermal energy to electrical energy is

$$\eta_{TE} = \eta_{TM}\eta_{ME} = \frac{\sum_{i=1}^{j} \eta_E \int_0^{t_e^i} (P_1^i - P_2^i) Q_{ac}^i dt}{c_{ps} m_{PCM}(T_s - T_0) + m_{PCM} L + c_{pl} m_{PCM}(T_e - T_l)} \tag{37}$$

However, the energy conversion efficiency cannot reflect the single cycle time of the thermoelectric generator. Long cycle time is not desirable. In addition, the overall mass of the system should not be too large. Therefore, another index need to be introduced. We take the average output power density $P_E$ within one cycle as an index to measure the energy performance, as defined in Eq. (38):

$$P_E = \frac{E_e}{(m_{PCM} + m_{MF} + m_{shell})(t_m + t_s)} \tag{38}$$

where $t_m$ and $t_s$ are the melting and solidification time of the PCM, respectively. $m_{PCM}$, $m_{MF}$ and $m_{shell}$ are the mass of the PCM, metal foam and the metal shell of the heat exchangers. The design of the wall thickness of heat exchangers accords with the pressure vessel standard: the relationship between the wall thickness $\delta$, maximum internal pressure $P_{imax}$, maximum external pressure $P_{emax}$ and the diameter of the chamber $d$ satisfies Eq. (39).

$$\delta \geq max\left( \frac{d}{\sqrt[3]{\frac{2E}{P_{emax}(1-\mu^2)}} - 2}, \frac{P_{imax} d}{2[\sigma] - P_i} \right) \tag{39}$$

where $E$ is Young's modulus, $\mu$ is Poisson's ratio, $[\sigma]$ is the yield strength. Due to the varying pressure of PCM during the melting process, take $P_{imax} = nP_2$, where $n$ is the safety factor and $P_2$ is system pressure at the beginning of power generation. $n$ takes a value of 2.5.

## 4. Experimental set-up and methods

### 4.1. Power generation experimental set-up and system identification method

#### 4.1.1. Power generation experimental set-up

The power generation efficiency model in Section 3.2 includes undetermined parameters ($k_1$–$k_{11}$), and system identification is needed

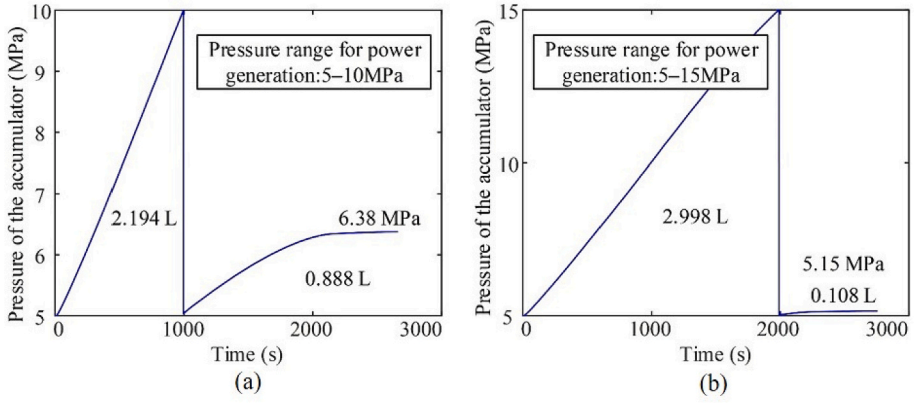


**Fig. 13.** Variation in accumulator pressure under different power generation pressure ranges at a pre charge pressure of 5 MPa: (a) pressure range for power generation: 5–10 MPa, and (b) pressure range for power generation: 5–15 MPa.

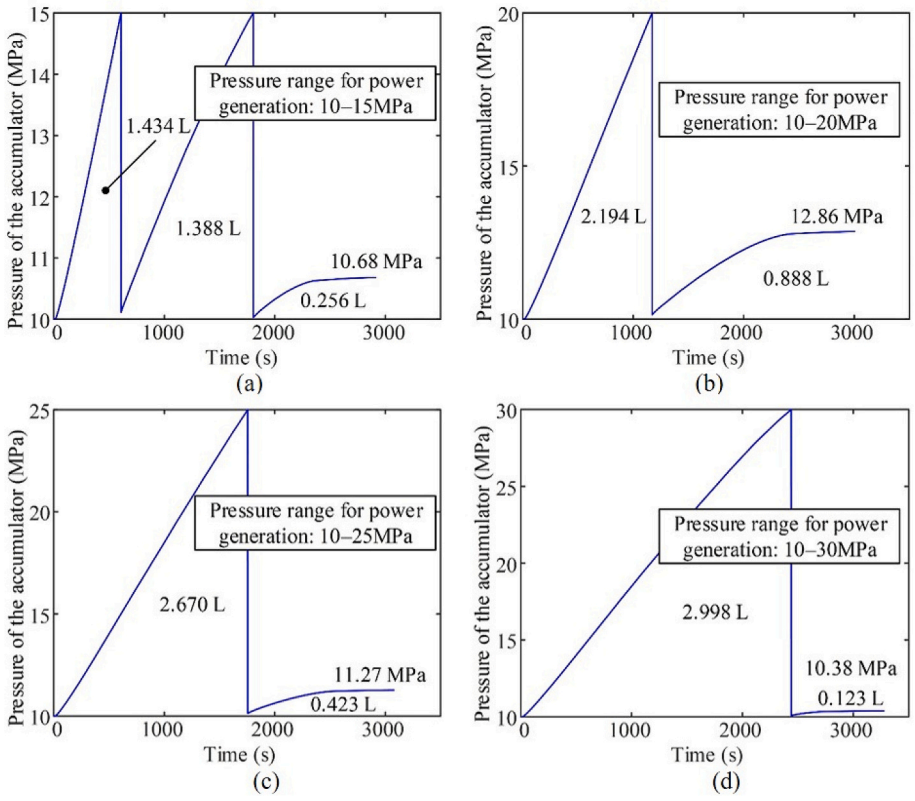


**Fig. 14.** Variation in accumulator pressure under different power generation pressure ranges at a pre charge pressure of 10 MPa: (a) pressure range for power generation: 10–15 MPa, (b) pressure range for power generation: 10–20 MPa, (c) pressure range for power generation: 10–25 MPa, and (d) pressure range for power generation: 10–30 MPa.

through experiments. Therefore, a power generation experimental set-up was built, as shown in Fig. 7. The accumulator in actual system is simulated by a hydraulic pump station, which can provide a stable pressure source for the power generation system. The inlet pressure of the hydraulic motor can be adjusted of and maintained stable by the hydraulic pump station. The relief valve is located between the outlet of the hydraulic motor and the return oil port of the hydraulic pump station, providing stable outlet pressure for the hydraulic motor, for simulation of external seawater pressure. The hydraulic motor is connected to the generator through a torque and speed sensor to monitor the torque and speed during the power generation process. Flow meters and pressure gauges were installed at the inlet and outlet of the hydraulic motor. The generator is connected to a rectifier to convert three-phase AC power into DC power. The actual Buck Boost circuit and rechargeable batteries were replaced by a programmable electronic load. The electronic load was set to constant current mode to regulate the current of the generator and output the generated voltage and current to the controller. The controller adjusts the speed of the hydraulic motor and generator by controlling programmable electronic loads. The closed-loop control of speed adopts the proportional integral derivative (PID) algorithm, and the speed can always remain stable at the set value during the power generation process.

The physical picture of the experimental set-up is shown in Fig. 7 (b), and the parameters of the components used in the experimental set-up are listed in Table 1.

#### 4.1.2. Experimental procedure

During the experiment, the outlet pressure of the hydraulic motor gradually increased from 0 MPa to 10 MPa at intervals of 2 MPa. Under constant outlet pressure, the speed range gradually increased from 400 rpm to 6000 rpm at intervals of 200 rpm and the inlet pressure increased from 5 MPa to 30 MPa at intervals of 1 MPa. The pressure, flow rate, speed, torque, voltage, and current data was recorded during power generation process.

#### 4.1.3. Error analysis

The uncertainty of the power generation experimental set-up is mainly caused by measurement errors of sensors, and the total relative uncertainty is given by:

$$U_c = \sqrt{\left(\frac{\sigma_{P_1}}{P_1}\right)^2 + \left(\frac{\sigma_{P_2}}{P_2}\right)^2 + \left(\frac{\sigma_{Q_1}}{Q_1}\right)^2 + \left(\frac{\sigma_{Q_2}}{Q_2}\right)^2 + \left(\frac{\sigma_T}{T}\right)^2 + \left(\frac{\sigma_n}{n}\right)^2 + \left(\frac{\sigma_U}{U}\right)^2 + \left(\frac{\sigma_I}{I}\right)^2} \times 100\% \quad (40)$$

The parameters and relative uncertainties of each sensor are listed in Table 2. The total relative uncertainty of the experimental set-up is calculated to be 1.07 %.

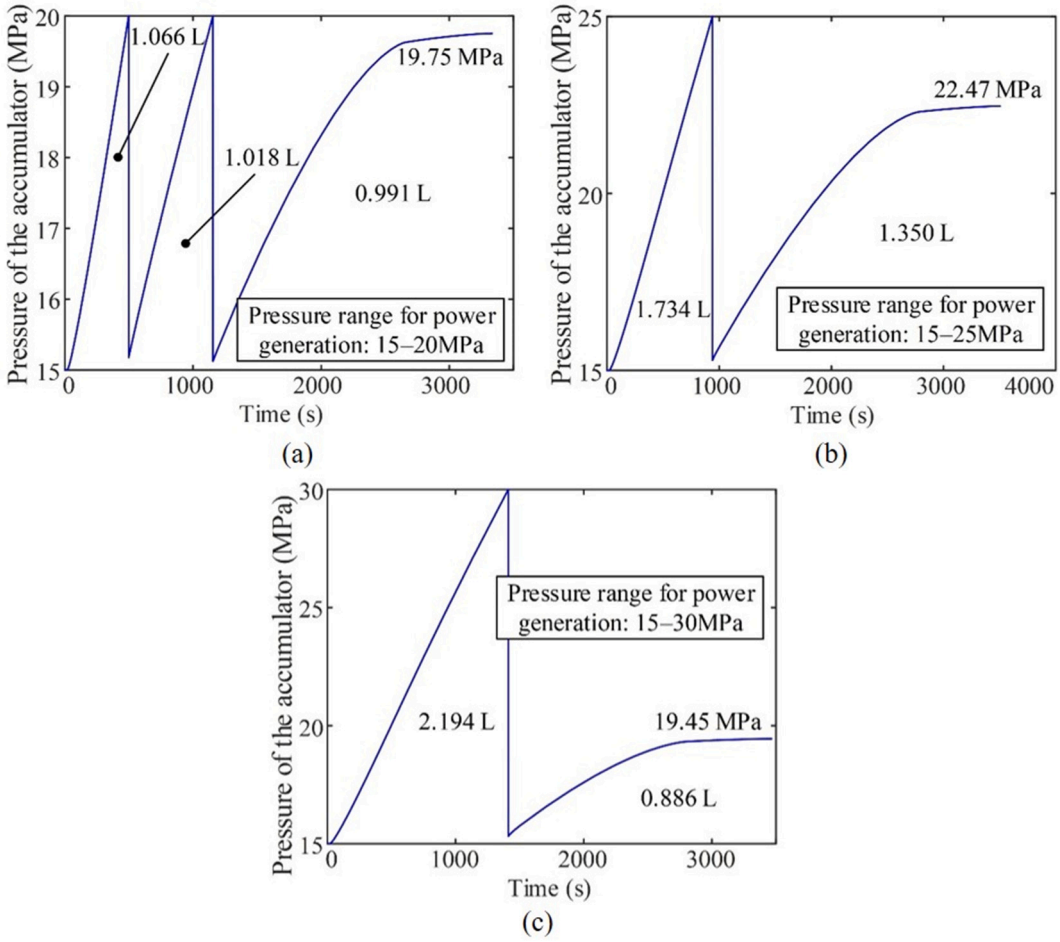


**Fig. 15.** Variation in accumulator pressure under different power generation pressure ranges at a pre charge pressure of 15 MPa: (a) pressure range for power generation: 15–20 MPa, (b) pressure range for power generation: 15–25 MPa, and (c) pressure range for power generation: 15–30 MPa.

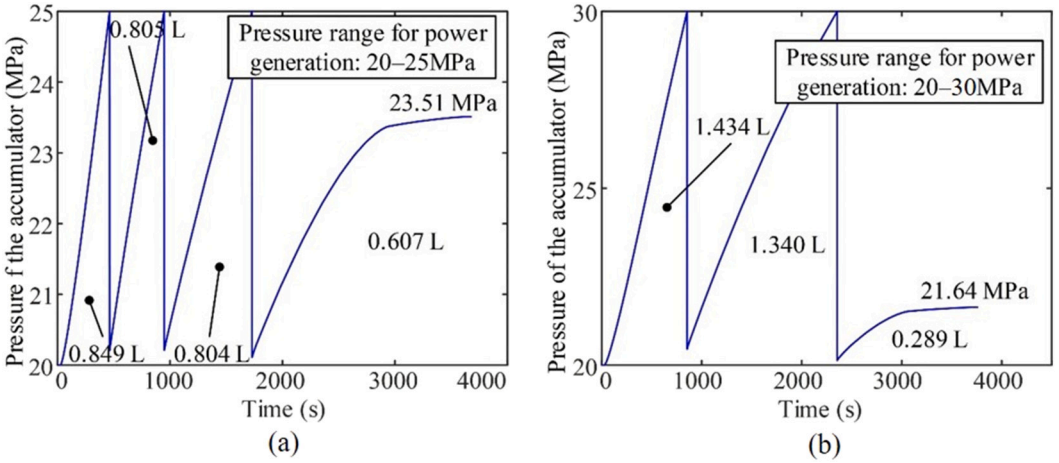


**Fig. 16.** Variation in accumulator pressure under different power generation pressure ranges at a pre charge pressure of 20 MPa: (a) pressure range for power generation: 20–25 MPa, and (b) pressure range for power generation: 20–30 MPa.

### *4.2. Ocean thermoelectric generator prototype and testing methods*

#### *4.2.1. Ocean thermoelectric generator prototype design*

We have developed a prototype of the ocean thermoelectric generator, as shown in Fig. 8. The prototype is equipped with various sensors inside, which can collect rich experimental data during the working operation. In the power supply circuit, the output end of the rectifier is connected to the input end of the rechargeable battery through a Buck Boost circuit. Relays were used as the switch for supplying power to the electrical components, and were controlled by the microcontroller unit (MCU). The sampling resistors are placed to monitor the generation voltage and current, charging voltage and current, battery voltage and current, and oil pump motor voltage and current through AD sampling. In the power generation system, the speed value obtained by the speed

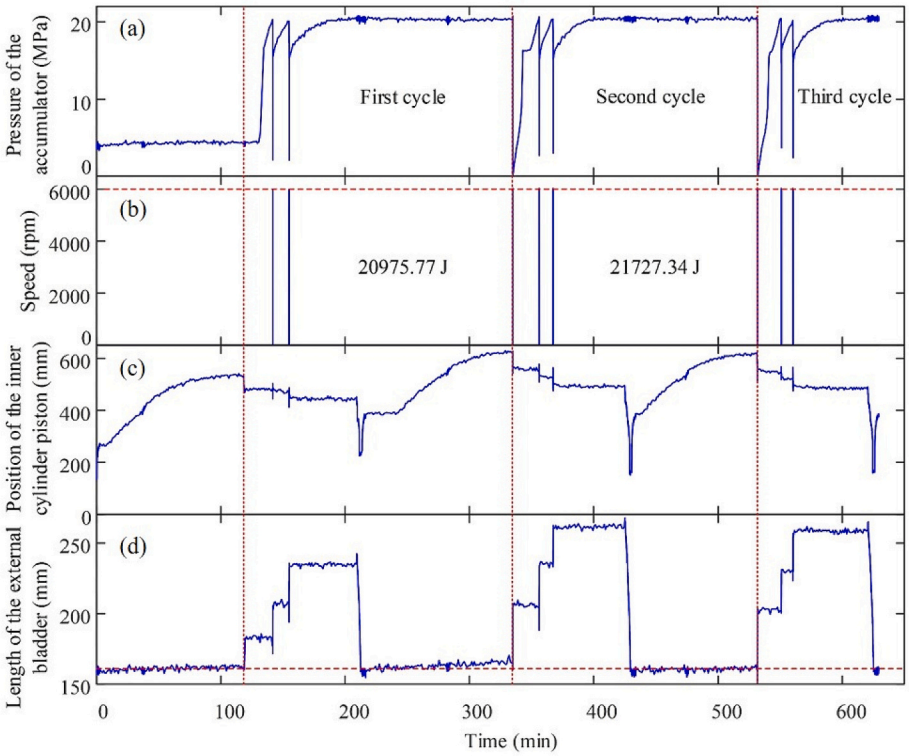


**Fig. 17.** Experimental results of the prototype: (a) pressure of the accumulator change, (b) generator speed, (c) position of the inner cylinder piston, and (d) length of the external bladder change with time.

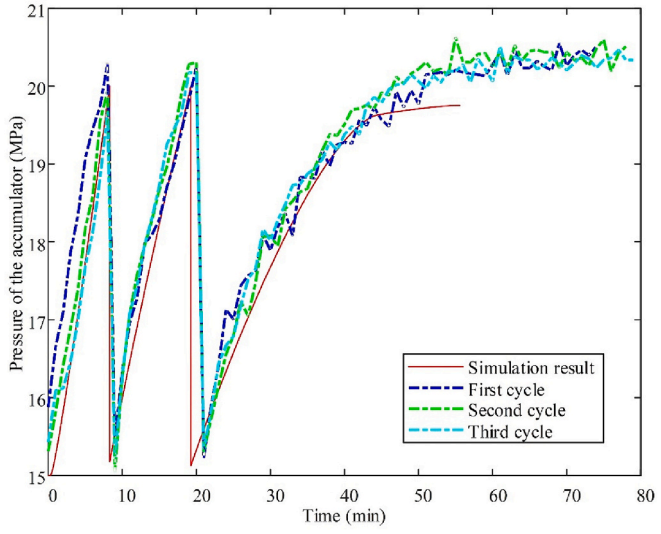


**Fig. 18.** Comparison between experimental and simulation results of accumulator pressure.

sensor is fed back to the MCU, and the main control outputs PWM to control the generator speed. The closed-loop control of speed is attained through proportional integral derivative (PID) algorithm, which is same as that in the power generation experiment set-up in Section 4.1.1.

As shown in Fig. 8 (b), the prototype test platform built in the laboratory is mainly composed of a water tank, a temperature controller, and a computer. The temperature in the water tank is regulated by the temperature controller, and the computer is connected to the MCU in the prototype to record data from the internal sensors.

Table 3 lists the relevant parameters of the heat exchangers and accumulator in the prototype. The prototype was equipped onto a underwater vehicle and the components of the total generator-vehicle system were weighed with an accuracy of 0.1 kg. The mass of each component is listed in Table 4.

**Table 1**
Parameters of the hydraulic pump station, hydraulic motor, and three-phase generator.

| Equipment | Parameter | Value |
|---|---|---|
| Hydraulic pump station | Maximum pressure | 63 MPa |
| | Maximum flow | 10 L/min |
| | Power | 11 kW |
| Hydraulic motor | Displacement | 0.4 cc/rev |
| | Rated inlet pressure | 30 MPa |
| | Maximum speed | 6000 rpm |
| Generator | Maximum power | 2000 W |
| | Maximum current | 43 A |
| | Maximum speed | 8500 rpm |
| | $K_V$ | 170 rpm/V |
| | $K_A$ | 0.042 N·m/A |
| | Internal resistance | 70 $m\Omega$ |

**Table 2**
Parameters and uncertainty of sensors used in the experimental set-up.

| Sensors | Range | Relative uncertainty |
|---|---|---|
| Inlet pressure sensor | 0– 40 MPa | 0.5 % |
| Outlet pressure sensor | 0–25 MPa | 0.5 % |
| Inlet flow meter | 0–10.8 L/min | 0.5 % |
| Outlet flow meter | 0–10.8 L/min | 0.5 % |
| Torque sensor | 0–5 N·m | 0.1 % |
| Speed sensor | 0–10,000 rpm | 0.1 % |
| Voltmeter | 0–120 V | 0.075 % |
| Ammeter | 0– 120 A | 0.35 % |

**Table 3**
Relevant parameters of the OTEng.

| | | |
|---|---|---|
| Heat exchangers | Inner radius (mm) | 55 |
| | Volume of the PCM (L) | 25 |
| | Filler | Copper foam with a porosity $\varepsilon$ of 95 % and pore density $\omega$ of 10 PPI |
| Accumulator PCM | Volume (L) | 5 |
| | Latent heat (J/kg) | 199,424 |
| | Specific heat capacity (J/kg·K) | 4046/3495 |
| | Phase-change region (K) | $T_s = 0.22571P + 285.4059$<br>$T_l = 0.16684P + 290.2882$ |
| | Thermal expansion coefficient (1/K) | 0.00089 |
| | Volume change rate | 13 % |

**Table 4**
The mass distribution of the underwater vehicle equipped with ocean thermoelectric generator.

| Component | Mass (kg) |
|---|---|
| Buoyancy material | 59.45 |
| Heat exchangers (10 pieces) | 93.8 |
| Supports | 2 |
| Hydraulic Components | 27.5 |
| End cap | 8.0 |
| Main chamber | 48.8 |
| Oil | 9 |
| Total mass | 251.5 |

#### 4.2.2. Experimental procedure

The prototype is placed in the water tank, and the temperature controller adjusts the temperature of the water tank to simulate the seawater temperature environment.

Initially, PCM is in the solid phase. First, the water temperature was set to 28 °C and maintained for 90 min to ensure complete melting of the PCM. During the melting process, the pressure reaches the maximum pressure, the on/off valve is opened, and the pressure inside the accumulator is released. Then the water temperature was set to 12 °C and maintained for 120 min to ensure complete solidification of PCM. Three identical cycles were conducted in the experiment.

## 5. Results and discussions

### 5.1. Results of the power generation experimental set-up

The efficiency of the power generation system $\eta_{ME}$ is discussed and analyzed using experimental data with an outlet pressure of 0 MPa, as shown in Fig. 9. When the pressure difference between the inlet and outlet of hydraulic motor $\Delta P$ is within the range of 5 MPa ~ 14 MPa, $\eta_{ME}$ first increases and then decreases with the increase of speed. Hence, there exists a peak efficiency. The peak efficiency and corresponding speed are positively correlated with $\Delta P$. When $\Delta P$ is between 15 MPa and 20 MPa, $\eta_{ME}$ decreases with the increase of $\Delta P$ at the same speed. Under the same $\Delta P$, $\eta_{ME}$ is positively correlated with the speed, and the slope of the $\eta_{ME} - n$ curve continuously decreases and approaches zero as the speed increases. Under high speed, $\eta_{ME}$ changes little and is between 50 % and 55 %. Therefore, the optimal speed for achieving maximum efficiency under $\Delta P$ of 15 MPa ~ 20 MPa is 6000 rpm. When $\Delta P$ is greater than 20 MPa, $\eta_{ME}$ is negatively correlated with $\Delta P$ at the same speed. $\eta_{ME}$ is positively correlated with the speed under the same $\Delta P$, and the slope of the $\eta_{ME} - n$ curve also decreases continuously with the increase of speed. However, the slope does not approach zero when reaching the maximum speed of 6000 rpm. Therefore, when $\Delta P$ is greater than 20 MPa, the optimal speed is still 6000 rpm. At this time, the maximum efficiency of the power generation system is between 42 % and 50 %.

**Table 5**
System identification results of the power generation efficiency model.

| | |
|---|---|
| $k_1$ | −0.19 |
| $k_2$ | 490.54 |
| $k_3$ | −19.25 |
| $k_4$ | −996.95 |
| $k_5$ | −0.0014 |
| $k_6$ | 0.013 |
| $k_7$ | −0.065 |
| $k_8$ | 4.55 |
| $k_9$ | 1196.93 |
| $k_{10}$ | 123.46 |
| $k_{11}$ | −4301.46 |
| Goodness of fit | 94.08 % |

The above experimental data under the outlet pressures of 0, 2, 4, 6, 8, and 10 MPa is used to identify the parameters in the power generation efficiency model (Section 3.2, Eq. (33)). The system identification results based on least square method are listed in Table 5. Note that the power generation efficiency $\eta_E$ cannot be negative, and is calculated according to Eq. (41).

$$\eta_E = max\left(\frac{k_1 n^2 + (k_2\Delta P + k_3 P_2 + k_4)n + (k_5\Delta P + k_6 P_2 + k_7)^2}{k_8\Delta P{\cdot}n + k_9\Delta P^2 + (k_{10}P_2 + k_{11})\Delta P}, 0\right) \tag{41}$$

To validate the accuracy of the efficiency model, another set of experiments were added: the outlet pressure was set to 5 MPa and the power generation efficiency under different pressure differentials were measured. The comparison between experimental data and simulation results of the efficiency model is shown in Fig. 10. The average relative error between two is 1.45 %, indicating the accuracy of the model.

Based on the power generation efficiency model, the optimal speed first increases linearly with the increase of $\Delta P$; When $\Delta P$ exceeds 13 MPa, the optimal speed remains unchanged at 6000 rpm, as shown in Fig. 11.

### 5.2. Results of the thermoelectric conversion simulation

The thickness of the ocean thermocline varies in different regions and seasons, within the range of 50-1000 m [27,28]. We divide the work environment into two categories: deep water areas (The thickness of the thermocline is around 500 m) and shallow water areas (The thickness of the thermocline is near to 50 m). In deep water areas, when an ocean thermoelectric generator descends into the cold-water area, the external water pressure and the amount of oil required for buoyancy regulation will increase and the energy loss for buoyancy regulation cannot be ignored. However, in shallow water areas, the oil required for buoyancy regulation is little and the outlet pressure of the motor is near to 0. Therefore, the energy consumed by buoyancy regulation can be ignored. In this section, different power generation strategies are analyzed based on the characteristics of different working areas.

#### 5.2.1. Power generation strategy in deep water areas

Power generation processes under diving depths of 500 m was analyzed. Firstly, it is necessary to determine the amount of oil required for buoyancy adjustment. The relation between sea water density and depth refers to [29]. Therefore, according to Eqs. (13)–(16), the minimum oil required for buoyancy adjustment for our developed prototype at depths of 500 m is 1.95 L. Note that the maximum volume change of phase change materials is 3.25 L. Therefore, in order to ensure the up and down movement of the total system, a single power generation strategy is adopted, that is, when the system descends to the set depth, the on/off valve is opened, and all the oil in the accumulator is used for buoyancy adjustment, flowing into the outer oil pocket.

The working cycle under different pre charging pressures were simulated. An accumulator with a nominal capacity of 5 L was used for

**Table 6**
Simulation results under different pre charging pressures and outlet pressures.

| Outlet pressure (MPa) | Pre charging pressure (MPa) | Phase change time (s) | Power generation (J) | $V_{oil,buo}$ (L) | $\eta_{TM}$ (%) | $\eta_{ME}$ (%) | $\eta_{TE}$ (%) | Power density (mW/kg) |
|---|---|---|---|---|---|---|---|---|
| 5 | 5 | 10,184 | 3237 | 1.99 | 0.78 | 0.11 | 0.083 | 4.74 |
| | 10 | 11,252 | 14,582 | 1.91 | 1.56 | 0.24 | 0.37 | 11.20 |
| | 15 | 14,083 | 23,611 | 1.70 | 2.35 | 0.26 | 0.61 | 9.87 |
| | 20 | 17,200 | 27,989 | 1.47 | 2.82 | 0.25 | 0.72 | 7.88 |

energy storage. The pre charging pressures of the accumulator were set to 5, 10, 15, and 20 MPa, respectively. To simulate environments at depths of 500 m in the deep sea, outlet pressure of hydraulic motor was set to 5 MPa. The effect of pre charging pressure on the melting process of PCM is shown in Fig. 12. As a comparison, the melting process under a pre charge pressure of 0.1 MPa was additionally calculated. The melting time is positively correlated with the pre charging pressure. The melting times under pre charging pressures of 0.1 MPa, 5 MPa, 10 MPa, and 15 MPa are 2395.5 s, 2984 s, 4051.5 s, and 6882.5 s, respectively. The increase in pressure significantly prolongs the melting time of PCM. When the pre charge pressure is 20 MPa, PCM cannot completely melt because the system pressure causes the melting point of the PCM to increase and exceed the ambient temperature.

The simulation results are listed in Table 6. Under the same outlet pressure, the power generation, total power generation, and conversion power are positively correlated with the pre charge pressure, while the volume of oil available for buoyancy adjustment and duration of power generation are negatively correlated with the pre charge pressure. This is because the higher pre charge pressure causes the hydraulic motor to have a greater pressure difference between inlet and outlet during power generation, resulting in a greater input power. However, the large pressure difference reduces the volumetric efficiency of the hydraulic motor, resulting in a shorter duration of power generation and a decrease in the amount of oil flowing into the external oil bladder.

As the pre charge pressure increases, the amount of work done by the PCM increases, causing an increase in the thermal–mechanical energy conversion efficiency $\eta_{TM}$. The mechanical–electrical energy conversion efficiency $\eta_{ME}$ is relatively low, because during the power generation process, the whole system is located in the deep sea, and there is a back pressure of 5 MPa at the hydraulic motor outlet; From the perspective of energy conversion, a portion of the mechanical energy in the accumulator is used for buoyancy regulation, resulting in a decrease in $\eta_{ME}$. The thermal–electrical energy conversion efficiency $\eta_{TE}$ is positively correlated with the pre charge pressure. However, as the pre charge pressure increases, the power density first increases and then decreases. This is because excessive pre charging pressure can cause an increase in the wall thickness of the heat exchangers, resulting in an increase in the weight; Meanwhile, the phase change time will also increase. Another drawback of high pressure is that it can lead to a reduction in $V_{oil,buo}$. This means that the hydraulic oil stored in the accumulator is not sufficient to drive the system for upward movement, so the system requires an additional buoyancy regulation system and the energy consumption of the buoyancy regulation with increase. Therefore, from the perspective of efficiency, the optimal pre charging pressure is 20 MPa, and from the perspective of power density, the optimal pre charging pressure is 10 MPa. Optimizing system parameters based on power density can be regarded as a compromise between efficiency, phase change time, and weight.

#### 5.2.2. Power generation strategy in shallow water areas

According to the analysis in Section 5.2.1, it can be concluded that in a single power generation strategy, as PCM continues to melt, and the pressure inside the accumulator gradually increases, greatly increasing the melting point, reducing the melting rate of PCM and even causing it to be unable to completely melt. Therefore, the pressure inside the accumulator can be released midway through the melting process to prevent excessive increase of pressure. This power generation strategy is referred to as the multiple power generation strategy in this paper. Through control program accordingly, when the pressure of the accumulator exceeds a certain value, the on/off valve is opened and the power generation process begins and the pressure of the accumulator decreases.

In numerical simulations, the pre charge pressures are set to 5 MPa, 10 MPa, 15 MPa, and 20 MPa, respectively. The pressures for starting power generation are set to 10, 15, 20, 25, and 30 MPa, respectively. The relationship between accumulator pressure and time for different pressure ranges with pre charging pressures of 5 MPa, 10 MPa, 15 MPa, and 20 MPa is shown in Figs. 13–16. By opening the on/off valve in a timely manner, the pressure of the accumulator will quickly drop to the pre charging pressure. Compared with single power generation strategy, when the pre charging pressure is increased, the multiple power generation strategy does not significantly increase the melting time.

The simulation results are shown in Table 7. Under different pressure ranges, $\eta_{ME}$ does not change much, and is in the range of 37 %–41 %, it is significantly higher than the energy conversion efficiency at a depth of 500 m. This is because buoyancy regulation hardly consumes energy. The system has the highest power density in the power generation pressure range of 15–20 MPa and 20–25 MPa. In our preliminary experiments, we found that high pressure increases the damage rate of Buck Boost circuit boards, and a lower range of power generation pressure can improve the reliability of the system. Therefore, 15–20 MPa is the optimal range of power generation pressure. Compared with the

**Table 7**
Simulation results under different multiple power generation strategies.

| Pre charging pressure (MPa) | The pressure to start power generation (MPa) | Phase change time (s) | Output electrical energy (J) | $\eta_{TM}$ (%) | $\eta_{ME}$ (%) | $\eta_{TE}$ (%) | Power density (mW/kg) |
|---|---|---|---|---|---|---|---|
| 5 | 10 | 9857 | 7596.40 | 0.52 | 37.35 | 0.20 | 15.60 |
| | 15 | 9950 | 9780.74 | 0.66 | 38.11 | 0.25 | 15.62 |
| 10 | 15 | 10,113 | 15,815.40 | 0.95 | 42.57 | 0.41 | 24.86 |
| | 20 | 10,204 | 17,142.70 | 1.04 | 42.07 | 0.44 | 21.83 |
| | 25 | 10,278 | 18,686.10 | 1.17 | 40.83 | 0.48 | 19.88 |
| | 30 | 10,476 | 20,239.15 | 1.32 | 39.30 | 0.52 | 18.14 |
| 15 | 20 | 10,533 | 22,955.20 | 1.36 | 43.14 | 0.59 | 28.32 |
| | 25 | 10,703 | 24,416.00 | 1.49 | 41.91 | 0.63 | 24.94 |
| | 30 | 10,666 | 25,036.60 | 1.57 | 40.91 | 0.64 | 22.04 |
| 20 | 25 | 10,877 | 28,248.60 | 1.75 | 41.36 | 0.72 | 28.39 |
| | 30 | 10,958 | 29,678.70 | 1.90 | 40.08 | 0.76 | 25.62 |

single power generation strategy, the power generation using an accumulator with a pre charging pressure of 15 MPa and a storage pressure range of 5 MPa for multiple energy storage has higher power generation efficiency and conversion power, and has significant advantages in small target depths.

### 5.3. Experimental results of the prototype

This section presents the experimental data of the prototype in a laboratory environment. The experimental set-up in Section 4.2 simulated the complete cycle process of the ocean thermoelectric generator in a shallow water area. The pressure range for power generation was set to 15–20 MPa. According to the results in Section 5.1, the speed for power generation in the pressure range of 15 MPa to 20 MPa is set to 6000 rpm. The experimental data was shown in Fig. 17 and was analyzed from two aspects: the thermal–mechanical and mechanical–electrical energy conversion process.

#### 5.3.1. Thermal–mechanical energy conversion process

During the melting process, the pressure change of the accumulator is shown in Fig. 17. The comparison between the experimental results and the simulation results in Section 5.2 is shown in Fig. 18. The two show good consistency, indicating the correctness of the energy conversion model proposed in Section 3.

Initially, there was still a small amount of residual hydraulic oil in the accumulator, so the accumulator pressure did not start from zero. When the water tank temperature is set to 28 °C, the phase change material continuously melted and the accumulator pressure first rapidly increases from the initial value to the pre charge pressure value and then slowly increases. Once the accumulator pressure surpasses 20 MPa, a single thermal-mechanical energy conversion process is completed, and the power generation system worked until the accumulator pressure drops below the pre-charge pressure. Due to the melting of PCM still ongoing, the accumulator pressure will quickly return to the pre charge pressure. In a complete cycle, there are three thermal-mechanical energy conversion processes. As the melting rate of PCM gradually decreased, the time of thermal-mechanical energy conversion process increased in sequence.

#### 5.3.2. Mechanical–electrical energy conversion process

At the beginning, the displacement sensor value of the external bladder decreased, resulting in negative net buoyancy of the system. The PCM solidified and sucked oil from the inner cylinder. The displacement sensor value inside the inner cylinder continued to increase. The data of power generation process are listed in Table 8. In the shallow water environment simulated in the laboratory, the outlet pressure of the hydraulic motor is near to zero. After one cycle, the output energy of the prototype was positive, achieving the energy self supply. The experimental and numerical results of the previous two power generation processes were compared. The relative errors between the power generation in the experiment and the simulation were 8.6 % and 5.3 %, respectively, indicating the accuracy of the power generation efficiency model.

Based on above experimental data, it can be calculated that $\eta_{TM}$ of the prototype is 1.128 %, $\eta_{ME}$ is 40.13 % and $\eta_{TE}$ is 0.453 %. The power generation density is 21.58 mW/kg. Note that the maximum efficiency of the thermal engine is limited by the Carnot theorem [30]. Under the conditions described in Section 4.2.2, this limit is given by:

$$\eta_{max} = 1 - \frac{T_{cold}}{T_{hot}} = 5.3\% \tag{22}$$

The experimental data on ocean thermoelectric generators in the literature is scarce. However, reference [31] documented the power generation of their prototype. The comparison between the prototype in this work and that in reference is shown listed Table 9. The developed prototype has reached international advanced levels in terms of energy efficiency and power generation density.

**Table 8**
Experimental data of the power generation system in the prototype.

| Cycle | Power generation | Output electrical energy (J) | Total power generation (J) |
|---|---|---|---|
| First cycle | 1st | 7308.93 | 20,975.77 |
| | 2nd | 6972.01 | |
| | 3rd | 6694.83 | |
| Second cycle | 1st | 7233.78 | 21,727.34 |
| | 2nd | 7120.29 | |
| | 3rd | 7373.27 | |
| Average value | / | 7117.18 | 21,351.55 |

**Table 9**
Comparison of the Prototype in this Study and existing literature.

| Reference | Power density (mW/kg) | $\eta_{TM}$ (%) | $\eta_{ME}$ (%) | $\eta_{TE}$ (%) |
|---|---|---|---|---|
| Reference [31] | n.d. | 0.9 | 44 | 0.396 |
| This work | 21.58 | 1.128 | 40.13 | 0.453 |

## 6. Conclusions

In this paper, detailed numerical and experimental research on the PCM-based ocean thermoelectric generator was conducted. In the experimental work, the parameters of the power generation system were identified and a prototype of a thermoelectric generator was developed. The experimental results of both the power generation system and the prototype have validated the correctness of the numerical model. The numerical calculation results and laboratory test data of the prototype were analyzed through energy efficiency and energy density. The specific conclusions are as follows:

(1) There exists an optimal speed to maximize power generation efficiency $\eta_E$. When the pressure difference $\Delta P$ between the inlet and outlet of the motor is less than 13 MPa, $\eta_E$ and $\Delta P$ are positively correlated; When $\Delta P$ is higher than 13 MPa, the optimal speed is 6000 rpm;
(2) When the thickness of the thermocline is around 500 m, a single power generation strategy needs to be adopted. An increase in pre charging pressure will improve energy efficiency, but also increase phase change time and system mass. From the perspective of maximizing power density, the optimal pre charging pressure is 10 MPa;
(3) When the thickness of the thermocline is low, multiple power generation strategies need to be adopted. The optimal power generation pressure range is 15-20 MPa;
(4) The developed prototype was tested in the laboratory environment, with a thermoelectric conversion efficiency of 0.453 % and a power density of 21.58 mW/kg, attaining state-of-the-art performance compared to the current literature.

The current study shows that the ocean thermoelectric generator can achieve a positive net output power, indicating that theoretically this equipment has an infinite working life. Therefore, ocean thermoelectric generators have great potential and will promote the development of long-term ocean observation technology in the future.

## CRediT authorship contribution statement

**Yanhu Chen:** Resources, Project administration, Funding acquisition. **Zesheng Yao:** Software, Investigation, Validation, Writing – original draft. **Bingzhe Chen:** Investigation, Methodology, Writing – original draft. **Canjun Yang:** Funding acquisition, Project administration. **Gul Muhammad:** Investigation. **Qingchao Xia:** Funding

acquisition.

## Declaration of competing interest

The authors declare that they have no known competing financial interests or personal relationships that could have appeared to influence the work reported in this paper.

## Data availability

Data will be made available on request.

## Acknowledgments

This work was supported by the National Natural Science Foundation of China (Nos. 52375032, 51979246 and 52205074), the National Key Research and Development Program of China (No. 2021YFC2800202), the Strategic Priority Research Program of Chinese Academy of Sciences (No. XDA22000000), the Science and Technology Innovation 2025 Major Project of Ningbo (2021Z079) and Science and Research Program of Zhejiang Province (No. 2021C03182).

## References

[1] S.M. Abbas, H.D.S. Alhassany, D. Vera, F. Jurado, Review of enhancement for ocean thermal energy conversion system, Journal of Ocean Eng. Sci. (2022), https://doi.org/10.1016/j.joes.2022.03.008. S2468013322000572.
[2] N. Khan, A. Kalair, N. Abas, A. Haider, Review of ocean tidal, wave and thermal energy technologies, Renew. Sust. Energ. Rev. 72 (2017) 590–604, https://doi.org/10.1016/j.rser.2017.01.079.
[3] M. Lin, C. Yang, Ocean observation technologies: a review, Chin. J. Mech. Eng. 33 (2020) 32, https://doi.org/10.1186/s10033-020-00449-z.
[4] M. Bianchi, I.F. Fernandez, A systematic methodology to assess local economic impacts of ocean renewable energy projects: application to a tidal energy farm, Renew. Energy 221 (2024) 119853, https://doi.org/10.1016/j.renene.2023.119853.
[5] R. Liu, L. He, X. Liu, S. Wang, L. Zhang, G. Cheng, A review of collecting ocean wave energy based on piezoelectric energy harvester, Sustain Energy Technol Assess 59 (2023) 103417, https://doi.org/10.1016/j.seta.2023.103417.
[6] G. Wang, Y. Yang, S. Wang, Ocean thermal energy application technologies for unmanned underwater vehicles: a comprehensive review, Appl. Energy 278 (2020) 115752, https://doi.org/10.1016/j.apenergy.2020.115752.
[7] D.C. Webb, P.J. Simonetti, C.P. Jones, SLOCUM: an underwater glider propelled by environmental energy, IEEE J. Ocean. Eng. 26 (2001) 447–452, https://doi.org/10.1109/48.972077.
[8] C. Jones, D. Webb, S. Glenn, O. Schofield, J. Kerfoot, J. Kohut, Slocum Glider extending the endurance, in: 16th Int. Symp. Unmanned Untethered Submers. Technol, 2009.
[9] C. Jones, B. Allsup, C. DeCollibus, Slocum glider: expanding our understanding of the oceans, in: 2014 Oceans - St. John's, IEEE, St. John's, NL, 2014, pp. 1–10, https://doi.org/10.1109/OCEANS.2014.7003260.
[10] Y. Yang, Y. Wang, Z. Ma, S. Wang, A thermal engine for underwater glider driven by ocean thermal energy, Appl. Therm. Eng. 99 (2016) 455–464, https://doi.org/10.1016/j.applthermaleng.2016.01.038.
[11] Y. Chao, Autonomous underwater vehicles and sensors powered by ocean thermal energy, in: OCEANS 2016 - Shanghai, IEEE, Shanghai, China, 2016, pp. 1–4, https://doi.org/10.1109/OCEANSAP.2016.7485367.
[12] C.D. Haldeman, O. Schofield, D.C. Webb, T.I. Valdez, J.A. Jones, Implementation of energy harvesting system for powering thermal gliders for long duration ocean research, in: OCEANS 2015 - MTS/IEEE Washington, IEEE, Washington, DC, 2015, pp. 1–5, https://doi.org/10.23919/OCEANS.2015.7404559.
[13] https://seatrec.com/news.
[14] J. Falcão Carneiro, F. Gomes de Almeida, Model of a thermal driven volumetric pump for energy harvesting in an underwater glider, Energy 112 (2016) 28–42, https://doi.org/10.1016/j.energy.2016.06.008.
[15] Q. Xia, Y. Chen, C. Yang, T. Zhang, Y. Zang, A new model of phase change process for thermal energy storage, Int. J. Energy Res. 42 (2018) 3877–3887, https://doi.org/10.1002/er.4120.
[16] G. Wang, Y. Yang, S. Wang, Thermophysical properties analysis of graphene-added phase change materials and evaluation of enhanced heat transfer effect in underwater thermal vehicles, J. Mol. Liq. (2021) 118048, https://doi.org/10.1016/j.molliq.2021.118048.
[17] Z. Ma, Y. Wang, S. Wang, Y. Yang, Ocean thermal energy harvesting with phase change material for underwater glider, Appl. Energy 178 (2016) 557–566, https://doi.org/10.1016/j.apenergy.2016.06.078.
[18] H. Kim, Towards the optimal operation of a thermal-recharging float in the ocean, Ocean Eng. 15 (2018).
[19] T. Liu, H. Sha, M. Li, M. Sun, G. Chen, D. Jiang, Y. Song, Theoretical analyses on a piston-based thermal engine for thermal underwater glider, Appl. Therm. Eng. 213 (2022) 118718, https://doi.org/10.1016/j.applthermaleng.2022.118718.
[20] Y. Chen, B. Chen, M. He, Experimental research of an ocean thermal engine with phase-change material, Appl. Therm. Eng. 210 (2022) 118363, https://doi.org/10.1016/j.applthermaleng.2022.118363.
[21] Y. Chen, Z. Yao, B. Chen, Z. Liu, C. Yang, Numerical and experimental study of the ocean thermal energy capture process utilizing metal foam–phase-change material (PCM) composites, Journal of Energy Storage 67 (2023) 107600, https://doi.org/10.1016/j.est.2023.107600.
[22] Z. Yao, C. Yang, B. Chen, G. Dai, Y. Chen, Computational fluid dynamics analysis of PCM-based ocean thermal engine with external rib turbulators, Appl. Therm. Eng. 238 (2024) 122054, https://doi.org/10.1016/j.applthermaleng.2023.122054.
[23] C.F.D. Direct Ltd, OpenFOAM v5 User Guide. http://openfoam.org, 2017.
[24] M. Aramesh, B. Shabani, Metal foam-phase change material composites for thermal energy storage: a review of performance parameters, Renew. Sust. Energ. Rev. 155 (2022) 111919, https://doi.org/10.1016/j.rser.2021.111919.
[25] A.D. Brent, V.R. Voller, K.J. Reid, Enthalpy-porosity technique for modeling convection-diffusion phase change: application to the melting of a pure metal, Numerical Heat Transfer 13 (1988) 297–318, https://doi.org/10.1080/10407788808913615.
[26] Y. Chen, B. Chen, M. He, L. Zhang, Q. Xia, C. Yang, Performance study of energy conversion system for ocean thermal profiler, Front. Mar. Sci. 9 (2022) 996204, https://doi.org/10.3389/fmars.2022.996204.
[27] G. Jin, Z. Tao, X. Liu, X. Zhuang, Analysis of temperature and salinity of sea based on Argo data, Mar. Environ. Sci. 29 (2010) 414–419.
[28] B. Zhao, A study on the basic characteristics and formation mechanisms of strong thermocline in the Bohai Sea, Yellow Sea, and Northern East China Sea, Acta Oceanol. Sin. 11 (1989) 401–410.
[29] M. Yang, S. Yang, Y. Wang, Y. Liang, S. Wang, L. Zhang, Optimization design of neutrally buoyant hull for underwater gliders, Ocean Eng. 209 (2020) 107512, https://doi.org/10.1016/j.oceaneng.2020.107512.
[30] G. Rogers, Y. Mayhew, Engineering Thermodynamics Work and Heat Transfer, fourth ed., Prentice Hall, Harlow, 1992.
[31] G. Wang, Y. Yang, S. Wang, H. Zhang, Y. Wang, Efficiency analysis and experimental validation of the ocean thermal energy conversion with phase change material for underwater vehicle, Appl. Energy 248 (2019) 475–488, https://doi.org/10.1016/j.apenergy.2019.04.146.